UC Irvine

UC Irvine Previously Published Works

Title

Test ion transport in a collisional, field-reversed configuration

Permalink

https://escholarship.org/uc/item/6q48p3r3

Journal

Plasma Sources Science and Technology, 23(4)

ISSN

0963-0252

Authors

Roche, T

McWilliams, R

Heidbrink, WW

et al.

Publication Date

2014

DOI

10.1088/0963-0252/23/4/044001

Copyright Information

This work is made available under the terms of a Creative Commons Attribution License, available at https://creativecommons.org/licenses/by/4.0/

Peer reviewed

eScholarship.org Powered by the California Digital Library
University of California

IOP Publishing Plasma Sources Science and Technology

Plasma Sources Sci. Technol. **23** (2014) 044001 (11pp) doi:10.1088/0963-0252/23/4/044001

Test ion transport in a collisional, field-reversed configuration

T Roche[1,2], R McWilliams[1], W W Heidbrink[1], N Bolte[1,2], E P Garate[1,2], M Morehouse[2], M Slepchenkov[2] and F Wessel[2]

[1] Department of Physics and Astronomy, University of California, Irvine, CA, USA
[2] Tri Alpha Energy, Inc., Rancho Santa Margarita, CA, USA

E-mail: troche@uci.edu

Received 18 July 2013, revised 3 March 2014
Accepted for publication 5 March 2014
Published 22 July 2014

Abstract

Diffusion of test-ions in a flux-coil generated, collisional, field-reversed configuration is measured via time-resolved tomographic reconstruction of Ar^+ optical emission in the predominantly nitrogen plasma. Azimuthal test ion diffusion across magnetic field lines is found to be classical during the stable period of the discharge. Test ion radial confinement is enhanced by a radial electric field, reducing the observed outward radial transport rate below predictions based solely on classical cross-field diffusion rates. Test ion diffusion is $\sim 500\ m^2\ s^{-1}$ during the stable period of the discharge. The electric field inferred from plasma potential measurements and from equilibrium calculations is consistent with the observed reduction in argon transport.

Keywords: transport, FRC, field-reversed configuration, test particle, cross-field, tomography, image reconstruction

(Some figures may appear in colour only in the online journal)

1. Introduction

The study of particle transport is integral to the ultimate success of fusion reactor experiments. Mitigation of energy and particle loss can only be accomplished once their mechanisms are well understood. Field-reversed configuration (FRC) [1] capabilities will benefit from further detailed transport studies. Various methods for experimentally determining transport rates in FRCs have been employed [2], but these results rely on inferences made from other measurements, i.e. changes in magnetic field strength and line-integrated density. Here, test particles [3] are introduced into the FRC and their evolution is observed so as to determine the plasma's diffusion coefficient across magnetic field lines in the azimuthal and radial directions. This direct, independent measurement allows the oft-used, rigid rotor model [4] to be compared for one experimental regime in terms of its transport predictions and its internal electric field predictions as well.

Test particles are commonly used to make localized measurements in plasmas. They can be impurities with low densities compared with the bulk plasma [5, 6] or a small fraction of the bulk plasma that has been modified such that their evolution can be tracked, as is the case in laser-induced fluorescence (LIF) [7]. Generally, the test particles interact with each other far less often than they do with the bulk plasma. Therefore, if we can observe their behavior, then we can infer properties of the plasma they are interacting with. The rotation of impurity and bulk plasma species can be in opposite directions. In this case, the rate of ion–ion collisions is fast enough and the rotational energy of the plasma is small enough compared with its thermal energy that we can assume the species rotate together [8].

This study is performed on the flux-coil generated FRC [9–12] (FCG-FRC). The temporal cross-field evolution of a test particle (argon) density distribution in a nitrogen plasma is observed. Through these observations we determine the argon's cross-field rate of diffusion and use that information to estimate the radial electric field, which is inherent in an FRC according to the rigid rotor model. The results are corroborated by independent measurements.

These measurements are obtained through the following sequence of events. An FRC is established using a backfill of nitrogen. A trace amount of argon is injected with a puff valve, at the midplane of the FRC, during formation,

 © 2014 IOP Publishing Ltd Printed in the UK

at the inner boundary. The evolution of the argon density profiles are determined via an optical tomography diagnostic [13]. The tomographic data result in 2D images that are further analyzed to determine both the azimuthal and radial components of argon's diffusivity. The FCG-FRC and important background theory as well as important information about classical diffusion and how an observed diffusion rate allows the ambipolar electric field to be determined in a classically behaving plasma are described in section 2. The implementation of the tomography diagnostic, in this system, is described in section 3. The results of the tomographic data are interpreted and compared with theoretical predictions in section 4. These results allow the FRC's radial electric field to be determined in a new way. This method, which relies on the ambipolar diffusion discussion, is described and verified through floating potential and magnetic field measurements in section 5. Conclusions are presented in section 6.

2. FRC description

2.1. Machine

The FCG-FRC is a cylindrical device where an FRC is formed between two concentric sets of coils. Gota *et al* [11], Gupta *et al* [10], and Slepchenkov *et al* [12] describe this device in more detail. The inner solenoid (flux-coil) is encased in a quartz tube with outer-diameter 17.1 cm which defines the inner boundary of the vacuum vessel. The outer boundary of the vacuum chamber consists of two coaxial pyrex tubes of diameter 61.4 cm which sandwich axially a polyethylene block capable of supporting many diagnostics. Total length of the system is 2.1 m. Sixteen outer coils are dispersed axially along the machine at $r = 42$ cm. They provide the confining magnetic field. Currents in the coils can be controlled independently [12]. A large (60 kA) current in the flux-coil induces a comparable plasma current, which reverses the magnetic field, establishing the FRC [14, 15]. The resulting magnetic fields are around $-200 \leqslant B \leqslant 200$ G.

In this method of FRC formation magnetic flux is added to the plasma on a slow time scale. The inner coil allows for a slow, inductive ramp-up of current in the plasma. The current in the outer coil is also increased to maintain pressure balance. The FRCs generated in this experiment undergo four stages of development: preionization, formation, equilibrium and collapse. These stages are best defined by the evolution of the magnetic field profile as a function of time. Figure 1 displays the time periods for the different stages typical of the shots examined here. In the preionization stage the nitrogen backfill of gas (~2 mTorr) is excited and ionized by ringing the central solenoid. Then a large capacitor bank is fired which drives current in the plasma causing field lines to reverse as can be seen in the formation stage. This reversal is maintained by a constant $\mathrm{d}I/\mathrm{d}t$ as the flux-coil current ramps up during the equilibrium stage. When the stored energy in the capacitor bank is depleted the field-reversal is lost and the plasma collapses under the pressure of the confining field in the collapse phase. The magnetic field is measured with a radial array of B-dot probes, at the midplane. The resulting

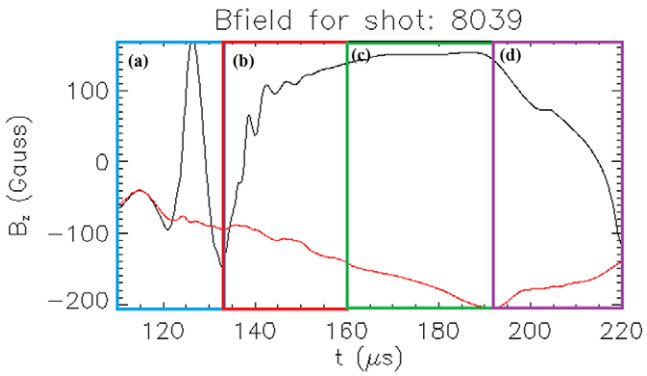

Figure 1. Four stages of FRC development: (*a*) preionization, (*b*) formation, (*c*) equilibrium and (*d*) collapse. The two traces represent the B_z component of the magnetic field, at the midplane near the inner (black) and outer (red) boundaries.

Table 1. Free parameters in rigid rotor model.

Parameter	Description
T	$T = T_\mathrm{i} + T_\mathrm{e}$ (Energy Units)
$\mathcal{N}_\mathrm{i}$	Number of ions per unit length
I_θ	Current per unit length
r_0	Radius of highest density
ω_i	Angular rotational frequency of ions
k	Unit-less shape factor

FRCs attain ion temperatures near 10 eV, electron densities in the range 0.5×10^{12}–1.0×10^{14} cm^{-3} and reversed fields in the range 100–300 G. These FRCs are relatively cold when compared with traditional theta pinch FRCs [1]. This results in a highly collisional environment. Thus, we expect the plasma to have classical transport properties.

2.2. Analytical framework

Under the assumption of a shifted-Maxwellian distribution function, a 1D, analytic solution to the Maxwell–Vlasov equations can be used to describe the structure of the FRC plasma near the midplane [4, 16]. The solution couples the density and electric/magnetic field profiles such that measurement of one determines the others. They take the form

$$B_z(r) = -\frac{2kcT\mathcal{N}_\mathrm{i}}{\pi r_0^2 I_\theta} \tag{1}$$

$$\times \left\{ \tanh\left[k\left(\frac{r^2}{r_0^2} - 1 \right) \right] - \frac{m_\mathrm{i}(\omega_\mathrm{i} r_0)^2}{4Tk} \right\}, \tag{2}$$

$$E_r(r) = -\frac{\langle\omega\rangle}{c} r B_z(r) - \frac{T_\mathrm{e}}{T}\frac{m_\mathrm{i}\omega_\mathrm{i}^2 r}{e}, \tag{3}$$

$$n_\mathrm{i}(r) = \frac{n_{i0}}{\cosh^2\left[k\left(\frac{r^2}{r_0^2} - 1 \right) \right]}, \tag{4}$$

with free parameters as described in table 1.

2.3. Classical transport

Before computing actual diffusion rates based on data we describe the classically predicted values for diffusion, with and

Table 2. Plasma physics parameters. $n_{avg} = 1.3e19\,m^{-3}$ and $B = 200\,G$ are used as the average plasma density and magnetic field strength in these calculations, respectively. Values under Larmor orbit period (τ_L) concern collisions between argon and the bulk plasma species. Test particle-test particle collisions are not considered. v_{th} is the thermal velocity. ω_c is the cyclotron frequency. ρ_L is the Larmor radius. λ_{mfp} is the mean free path between collisions. τ_{col} is the ion–ion collisional period.

Quantity	Units	Equation	Nitrogen	Argon
Mass	kg		$14\,m_p$	$40\,m_p$
T	eV		10	10
v_{th}	$m\,s^{-1}$	$\sqrt{\frac{2k_BT}{m}}$	1.17×10^4	6.92×10^3
ω_c	$Rad\,s^{-1}$	$\frac{eB}{m}$	1.37×10^5	4.8×10^4
ρ_L	m	$\frac{v_{th}}{\omega_c}$	8.54×10^{-2}	1.44×10^{-1}
τ_L	s	$\frac{2\pi}{\omega_c}$	4.58×10^{-5}	1.31×10^{-4}
$\nu_{Ar,j}$	Hz	See NRL [17]	5.38×10^4	
λ_{mfp}	m	$\frac{v_{th,Ar}}{\nu_{Ar,j}}$	0.129	
τ_{col}	s	$\frac{1}{\nu_{Ar,j}}$	1.86×10^{-5}	
μ	$m^2\,V^{-1}\,s^{-1}$	$\frac{e}{m\nu_{Ar,j}}$	34.5	
D	$m^2\,s^{-1}$	$\frac{v_{th,Ar}^2}{2\nu_{Ar,j}}$	445	
$\omega_{c,Ar}^2\tau_{col}^2$	—	—	0.794	
$\mu_\perp$	$m^2\,V^{-1}\,s^{-1}$	$\frac{\mu}{1+\omega_{c,Ar}^2\tau_{col}^2}$	23.3	
$D_\perp$	$m^2\,s^{-1}$	$\frac{D}{1+\omega_{c,Ar}^2\tau_{col}^2}$	248	

without a magnetic field, given the plasma parameters on this FRC. Table 2 is a description of the relevant plasma parameters necessary to compute the classical transport coefficients. The items which have no value (in table 2), under the argon column, relate to the collision processes where argon is considered the 'test particle', and the element in the column header is the 'field particle'. For instance, the value of $\nu_{Ar,j}$ under the nitrogen column is the rate at which an argon test particle collides with a background of nitrogen plasma, i.e. an ion–ion collision.

The Coulomb ion–ion collision rate, ν_{ii}, is directly proportional to the plasma density [17]. The values in table 2 are computed using the average ion density (n_i) during the equilibrium phase. Therefore, $\nu_{Ar,j}$ is actually radially dependent according to equation (4). The strength of the perpendicular magnetic field affects the value of $D_\perp$. We calculate $D_\perp$ using plasma parameters, which has no θ dependence (due to θ symmetry of FRC). $D_\perp$ is the same in both radial and azimuthal directions because it only represents the collisionally driven diffusion, and does not consider the electric field described in equation (3). However, $D_\perp$ does depend on the radial position since the axial magnetic field is near zero at r_0 and its magnitude increases when moving radially away from r_0.

2.4. Effect of electric field on diffusion

The radial electric field predicted by the rigid rotor model in equation (3) will modify the observable rate of diffusion in the radial direction. Depending on whether the electric field points toward or away from the null radius the observable diffusion coefficient for ions will either increase or decrease, respectively. Manipulation of the fluid equations of motion, for a plasma with magnetic and electric fields present, leads to an argon test particle flux of [18]:

$$\boldsymbol{\Gamma}_\perp = n_i\,\mu_\perp \boldsymbol{E} - D_\perp \nabla n. \tag{5}$$

We also know from Fick's laws that [19]

$$\boldsymbol{\Gamma}_{obs} = -D_{obs}\,\nabla n. \tag{6}$$

D_{obs} on the right-hand side of the equation (6) is the total, or observable, diffusion. In an FRC D_{obs} will be different in radial and azimuthal directions due to the radial electric field. $D_\perp$ in equation (5) is related to the diffusion process that comes purely from the collisions between particles. In equation (6), the effects of the electric field are macroscopically integrated and thus, indistinguishable from the collisions, but they are both responsible for particle flux. Therefore, equating equations (5) and (6), and assuming that the plasma behaves classically, i.e. $D_\perp$ has the value for diffusion calculated in section 2.3, another (recall equation (3)) independent expression for the electric field is realized. It is

$$\boldsymbol{E} = \frac{D_\perp - D_{obs}}{\mu_\perp}\frac{\nabla n}{n}. \tag{7}$$

This assumes that $D_\perp$ is isotropic, but considering the highly collisional nature of the plasma in this experiment, this is likely the case.

3. Optical tomography

Optical tomography is an image reconstruction method. It uses multiple 1D line of sight measurements to reconstruct a 2D image. There are a variety of methods which lead to the 2D image. Some are analytical and others rely on numerical, matrix-inversion techniques [20]. The analytical methods involve Fourier analysis of the mode structure of the image. When lines of sight are limited (to say <100), numerical methods provide useful information.

3.1. Analytics

The inversion technique employed in this work is called minimum Fisher regularization (MFR). It was developed by Anton *et al* [20] as a hybrid of linear regularization (LR) and minimum Fisher information (MFI). The basic idea is to solve the following set of equations:

$$f_l = \int_{S_l} \mathrm{d}s\, g(\boldsymbol{r}) \qquad l = 1 \ldots n_l, \tag{8}$$

where the f_l are the (relatively) calibrated photomultiplier tube (PMT) signals and $g(\boldsymbol{r})$ is the emissivity of the plasma.

We discretize $\boldsymbol{g}$ by breaking the space into square pixels. There are n_x pixels in the horizontal direction and n_y pixels in the vertical direction for a total of $n_{\text{pixels}} = n_x \times n_y$. $\boldsymbol{g}$ and $\boldsymbol{f}$ become column vectors with n_{pixels} and n_l rows, respectively. Then, equation 8 becomes

$$\boldsymbol{f} = \boldsymbol{T} * \boldsymbol{g}, \tag{9}$$

where $\boldsymbol{T}$ is a matrix which contains the geometric information of the lines of sight, such that

$$T_{li} = \int_{S_{li}} \mathrm{d}s. \tag{10}$$

In other words, T_{li} represents the length of chord l inside pixel i. Generally speaking, direct inversion of $\boldsymbol{T}$ is not possible. Either there are very few equations, i.e. $\boldsymbol{T}$ is not invertible or, even if we had $n_{\text{pixels}} = n_l$, $\boldsymbol{T}$ is poorly conditioned (very sparse). Resolution of this issue is two-pronged. First, we employ LR to couple adjacent pixels together. Second, minimum Fisher information is applied, iteratively, to further refine the coupling between pixels. This produces the best reconstructions possible with the limited number of chords available. With these tools in place we seek to minimize

$$\phi = \tfrac{1}{2}\,(\tilde{\boldsymbol{T}} * \boldsymbol{g} - \tilde{\boldsymbol{f}})^{\mathrm{T}} * (\tilde{\boldsymbol{T}} * \boldsymbol{g} - \tilde{\boldsymbol{f}}) + \alpha \boldsymbol{g}^{\mathrm{T}} * \boldsymbol{H} * \boldsymbol{g}, \tag{11}$$

where ϕ is χ^2 for the system with the smoothing matrix, $\boldsymbol{H}$, incorporated. The tildes represent division by the standard deviation of f_l, i.e. $\tilde{f}_l = f_l/\sigma_l$. The weights are determined by equation (12) through successive iterations of the reconstruction process.

$$W_{ij}^{(n)} = \begin{cases} \dfrac{1}{2\, g_i^{(n)} g_i^{(n-1)}} \cdot \delta_{ij} & g_i^{(n)} > 0 \quad n > 0 \\ W_{\max} \cdot \delta_{ij} & g_i^{(n)} \leqslant 0 \quad n > 0. \end{cases} \tag{12}$$

$W_{\max}$ is a maximum weighting value used for those pixels which have erroneously been determined to be negative. $W_{\max}$ is simply $1/g_{\min}$ for $g_i > 0$. The smoothing matrix becomes

$$\boldsymbol{H} \to \boldsymbol{H}^{(n)} = \Delta^{\mathrm{T}} * \boldsymbol{W}^{(n)} * \Delta, \tag{13}$$

This leads to the system of equations to be solved:

$$(\tilde{\boldsymbol{T}}^{\mathrm{T}} * \tilde{\boldsymbol{T}} + \alpha \boldsymbol{H}^{(n)}) * \boldsymbol{g}^{(n+1)} = \tilde{\boldsymbol{T}}^{\mathrm{T}} * \tilde{\boldsymbol{f}}, \tag{14}$$

where we have set all of $\partial\phi/\partial g_i = 0$. We solve equation (14) for $\boldsymbol{g}$ using the commonly applied method of lower/upper triangular (LU) decomposition [21]. A more complete derivation of these equations is available in [20].

3.2. Experimental arrangement

The basic design principle for the tomography diagnostic consists of two fan arrays with eight collimated lines of sight each. The light incident on each collimator lens is focused onto a fiber, with numerical aperture of 0.22, which transmits light through a series of filters, and is finally measured by 1 of 16 PMTs. The acceptance angle of each line of sight is $\sim 1^\circ$.The general setup of light collection apparatus is shown in figure 2.

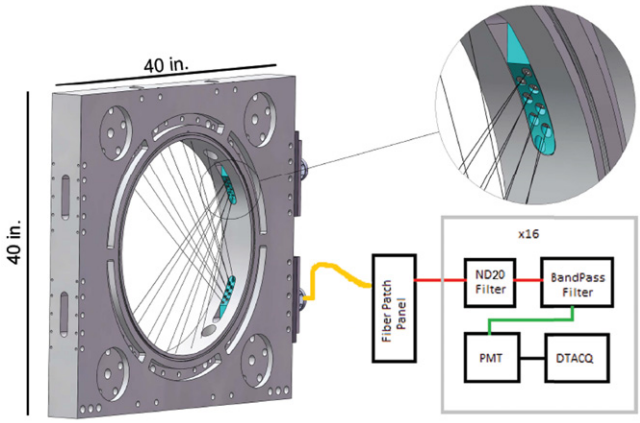

Figure 2. A schematic of the tomographic diagnostic. Each fan consists of eight lines of sight of which there are two. Each collimator/lens/fiber arrangement is set flush with the outer boundary. Every line of sight has $\sim 1^\circ$ acceptance angle. All of the signals are routed through a series of filters and onto a PMT. The PMTs' outputs are recorded by digital oscilloscopes.

Specific information about the diagnostic's implementation is found in [13]. The argon gas is introduced into the system in a highly localized manner by means of a fast puff valve (which is separate from the nitrogen backfill system) and a long tube that runs along the interior boundary to the midplane of the machine. The end of the tube is positioned such that the argon flows directly into the center of the tomography diagnostic's view. The puff valve is activated so that the gas arrives just after the FRC forms. In this case, the filters are designed to only transmit light from the Ar^+ spectral line at 434.8 nm to the PMTs. Argon works in this system but, in principle, another impurity could be chosen depending on target's plasma parameters. Like the bulk plasma species (nitrogen) the argon is singly ionized due to the relatively low electron temperature. This is verified by observing spectral lines from the two species for singly and doubly ionized states. Strong lines for singly ionized states are bright enough to saturate PMT detectors on a spectrometer while the doubly ionized lines are virtually undetectable.

Using the geometry of the lines of sight in figure 2 simulated data are produced to gauge the effectiveness of the tomographic reconstruction algorithm. The number of successive iterations that must be performed on the experimental data is determined by looking at successive reconstructions of simulated input data as shown in figure 3. The reconstruction converges after four iterations. Two fans of eight chords each are arranged such that the lines of sight form a mesh as depicted in the lower left corner of figure 3 which matches the physical experiment's geometry.

4. Diffusion analysis

In this section the data gathered with the diagnostic described in section 3 are analyzed to determine the FRC's rate of diffusion. The test ion density profile is reconstructed, at 1 μs intervals, over the lifetime of the FRC. The generated images are both the output of the tomography algorithm, and the starting point

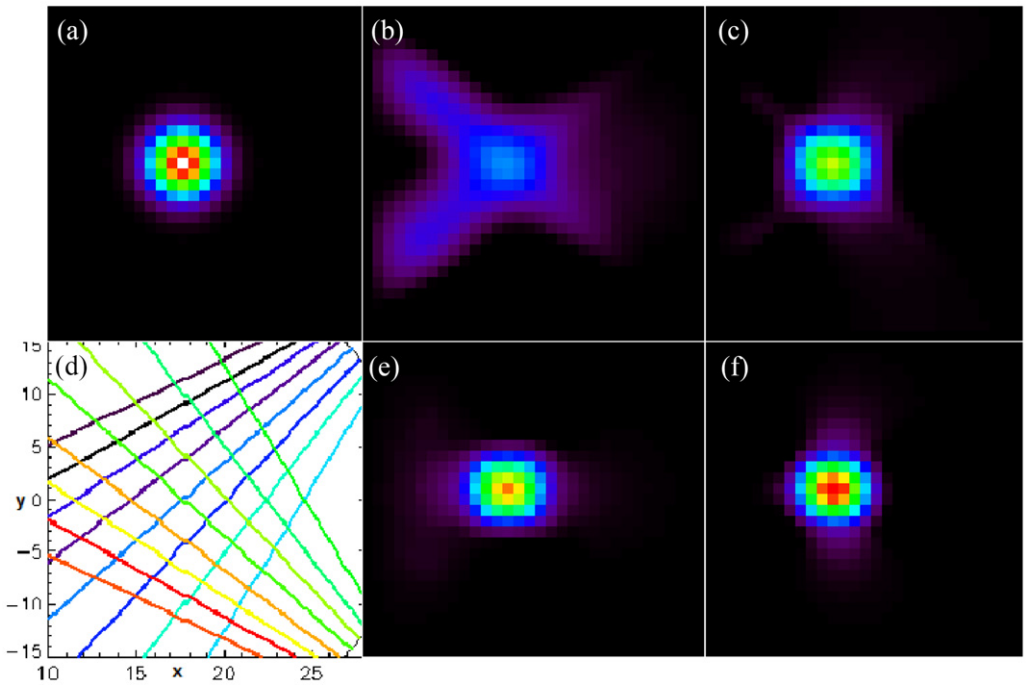

Figure 3. Simulation with Gaussian input. (*a*) Input image. (*b*), (*c*), (*e*), (*f*) Successive iterations of the algorithm using simulated data for the input image as would be collected using the experimental detection chord geometry. Notice how the iterative weighting recovers not only the shape, but the peak height of the input. (*d*) Representation of line-of-sight coverage, 16 chords in total. These are the chords used to reconstruct the images in (*b*), (*c*), (*e*) and (*f*). They are also used to calculate line-integrated values from (*a*) which are used as the inputs to the reconstruction algorithm.

of the physics discussion to follow. The spatial resolution of the diagnostic is 1 cm × 2 cm, which is optimal in terms of FRC feature sizes and computational requirements.

4.1. Observed diffusion

D_{obs} is the diffusion coefficient as calculated strictly from the observation of tomographic data alone. This observed diffusion coefficient comes directly from experimental measurement, and not from any inferences dependent on the plasma physics. The value determined is representative of the total particle flux (of the test ion population), and includes any transport-altering effects due to electric fields. For example, an electric field pushing particles toward the center of the FRC would reduce the outward observed diffusive flux as inward convection offsets outward diffusion. We calculate D_{obs} in both cross-field, orthogonal directions ($\hat{\boldsymbol{\theta}}$ and $\hat{\boldsymbol{r}}$). These two coefficients are determined independently, since the radial electric field causes the observed values to differ.

If a Gaussian distribution diffuses in a one-dimensional process in time, according to Fick's first law [19]:

$$\boldsymbol{\Gamma} = -D\,\boldsymbol{\nabla} n, \tag{15}$$

then the diffusion coefficient goes like the change in the full width of the Gaussian at half of its maximum (FWHM) squared, divided by the change in time or

$$D = \frac{1}{16\ln 2}\frac{\partial\left(\text{FWHM}^2\right)}{\partial t}. \tag{16}$$

So to calculate D_{obs}, the observed test particle density profile is fit to a Gaussian, at each time step, and the derivative is calculated with respect to time. The Gaussian takes the form:

$$f(x) = A_0\,\text{Exp}\left(-\frac{(x-x_0)^2}{2\sigma^2}\right) \tag{17}$$

and

$$\text{FWHM} = 2\sqrt{2\ln 2}\,\sigma, \tag{18}$$

where x can represent the radial (r) or azimuthal ($r_{\text{max}}\cdot\theta$) coordinate and r_{max} is the radius of greatest density according to the reconstructed profile.

4.2. Case selection

Half of the shots on which tomographic analysis is performed exhibit purely diffusive behavior. Some shots exhibit behavior that cannot be quantified by simple Gaussian diffusion. Their characteristics included: filamentation, convection and axial wobble. The particular case described in this section represents the FRC with the most stable equilibrium phase and best signal-to-noise ratio, with respect to the optical signals. Other comparable shots have similar results. In addition to a primarily nitrogen plasma, a primarily hydrogen plasma is also studied. Although the hydrogen FRCs are typically shorter lived, the diffusion analysis produces similar results.

Figure 4 shows both the raw and conditioned data from a single PMT channel on shot 8039. The error in the PMT measurements is taken to be the standard deviation of the signal

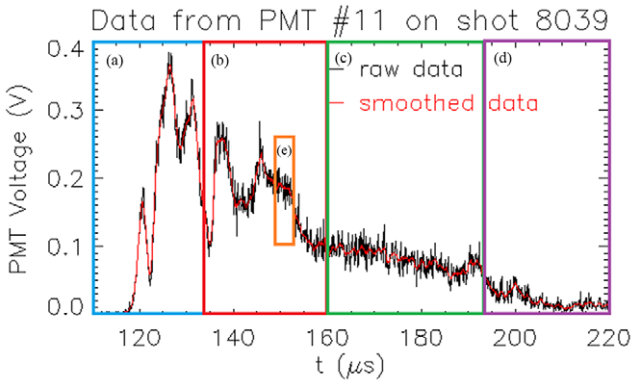

Figure 4. Single channel raw and smoothed data to be used as input for image reconstruction algorithm. The data are divided into the same sections as in figure 1: (*a*) preionization, (*b*) formation, (*c*) equilibrium, (*d*) collapse. (*e*) represents the time period of the reconstructions in figure 5.

over the period of time (1 μs) between interpolated values. These errors are the ones used in equation (11).

After the data have been conditioned, they are fed into the reconstruction algorithm. Each time slice is treated independently. Therefore, apart from the temporal smoothing (on the preprocessed data) there is no smoothing of the output images in the time dimension. A short time window has been selected in figure 5. Here the evolution of the test ion density profile can be observed over the course of a few microseconds. The white lines represent the various lines of sight. The line of sight highlighted in red is PMT #11. Its raw data are displayed in figure 4.

4.3. Diffusion in the Azimuthal direction

To determine $D_{\mathrm{obs},\theta}$ we fit Gaussian profiles to the azimuthal arc that intersects the point of highest density. This radius is referred to as $r_{\max}$. The density peak is determined by examining the reconstructed image (at each time slice) of the emissivity profile. An arc is drawn with radius $r_{\max}$ and is bound by the outermost lines of sight (white lines in figure 6). $n(r)$ (or $\epsilon(r)$) is determined along this arc (one point per pixel), and those points are fit to a Gaussian. An example of one of the azimuthal fits is displayed in figure 6. The error estimates on the data in figure 6 come from the short-timescale (2.5 μs) variation of the calculated pixel emissivity. Any long-timescale trend is removed, then the standard deviation of these data is taken to be the error for the associated datum. Only fits with reduced $\chi^2 < 2$ are used in the calculation of D_{obs}.

Doing Gaussian fits to the time-dependent data provides the full-width half-maximum (FWHM) versus time as shown in figure 7. Finding the observed diffusion coefficient by means of equation (16) leads to $D_{\mathrm{obs},\theta}$ versus t, as illustrated in figure 8. The values for the error bars are calculated using the statistically weighted error estimates from the previously performed Gaussian fits. The errors are propagated forward in the usual way.

Toward the end of the formation period and into the start of the equilibrium phase (near 150–155 μs in the time window shown in figure 8) the azimuthal cross-field diffusion coefficient is in the range 200–500 $\mathrm{m^2\,s^{-1}}$, about classical to three times classical diffusion predictions (see table 2). For azimuthal diffusion near the null, magnetic effects on D are reduced and the classical expected value of D would be predicted to be somewhere between the $B = 0$ value of $D \sim 500\,\mathrm{m^2\,s^{-1}}$ and the $B = 200\,\mathrm{G}$ value of $D \sim 250\,\mathrm{m^2\,s^{-1}}$.

4.4. Diffusion in the radial direction

Calculating the radial cross-field component of the diffusion coefficient is very similar to the azimuthal part. The difference is the Gaussian fit is performed along a radial chord which intersects the density peak. A line is drawn from $r = 0$ through the pixel whose density (or emissivity) is maximum and a Gaussian is fit to the values of the pixels which intersect it. As before, the detrended, short-timescale, statistics determine the error bars (figure 9). The rest of the procedure is identical. A plot of the radial FWHM versus time is illustrated in figure 10. Figure 11 shows the equilibrium time $D_{\mathrm{obs},r}$ is near zero or even negative.

During formation radial diffusion is less than classical values and during equilibrium (160–180 μs) the observed radial diffusion drops further, even becoming negative. This means that the ions are being propelled radially toward the FRC null radius, and the test particle density profile is peaking up. This behavior is due to the radial electric field (section 2.2). An example of the electric field profile is displayed in figure 12. Note that this field is confining for ions.

5. Radial electric field determination

The radial electric field, predicted by the rigid rotor model [4], proves to be integral in the understanding of the radially directed diffusion. The discrepancy, between D_{obs} and $D_{\perp}$, is eliminated when the convective effects of the electric field are considered. In this section we present data of measurements of the electric field (via direct measurements of the floating potential); and compare the theoretically predicted, experimentally measured and tomographically implied fields.

The density profile must be known to calculate $\boldsymbol{E}$ from equation (7). Either the Gaussian fit made to the tomographic data or the density profile determined by the magnetic field could be used to make this calculation. Both are reasonable choices; the former would be more appropriate if it is desired to keep estimates completely independent. On the other hand, the Gaussian fit is really only reliable within $1/e$ of the density peak. It approaches zero rather quickly and thus $\nabla n/n$ does not reflect properly the physical situation far away from the density peak. This is not the case for the rigid rotor model density profile [4], which goes like $1/\cosh^2$.

5.1. Electric potential/field measurements

In order to verify the proposed theoretical interpretation of this diffusive process the electric field must be physically measured. Direct measurement of the floating potential (V_{f}) is performed using a floating tip probe (figure 13). The probe itself consists of a $\frac{1}{4}$ inch glass tube with 2–1.5 mm tips spaced

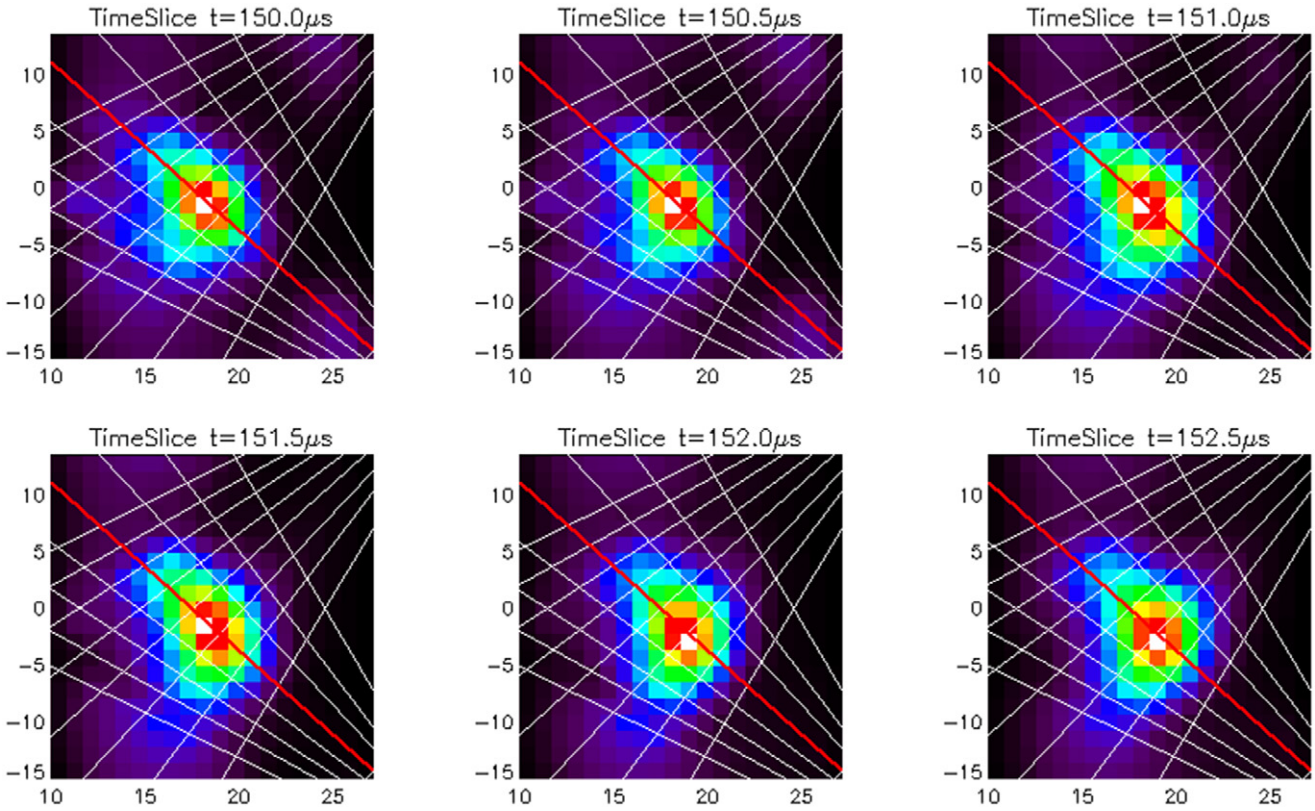

Figure 5. Slow evolution of test ion density profile as a function of time: Shot 8039. White lines represent line of sight paths. Red line is PMT #11.

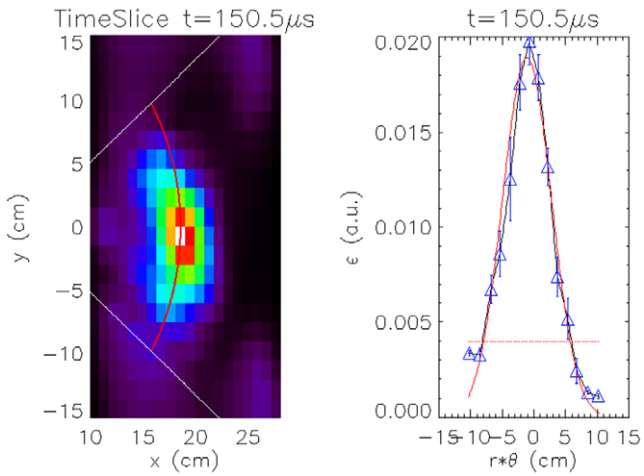

Figure 6. Example of a Gaussian fit along an azimuthal arc (right) which intercepts the point of highest density and the associated 2D density profile (left). The blue triangles represent the data points and their associated errors. The solid red line is the Gaussian fit (right). The dashed red line is the cutoff value. Any data with values below this line are not included in the Gaussian fit.

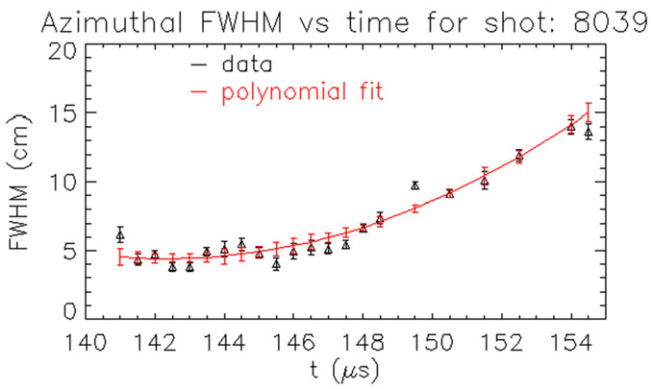

Figure 7. Time evolution of the azimuthal width of the test ion density profile for shot 8039. The black triangles represent the FWHM from the Gaussian fits at each time slice. The red line is a polynomial fit to the experimentally measured values. Gaps in the data are due to times when the reduced χ^2 of the Gaussian fits are greater than 2.

6 mm apart protruding out of the tube near the end of the probe. Initially, the probe was constructed to measure the local electric field between the two tips. However, at the time of experiment, the electronics for measuring the differential signal did not function correctly and the potential at each tip was measured independently. Since T_e is mostly flat inside the FRC, the radial electric field can be inferred from the V_f measurements.

The measurements are made over a series of shots at multiple radial locations. Six shots are taken at each position, with V_f measured on one tip for three of those shots and the other tip for the other three. Forty-five shots are taken for a total of 15 distinct radial positions. The circuit used for measurement is a very simple voltage divider and line driver. This circuit reduces the signal to levels required by, and preserves the integrity of the signal as it travels to, the data acquisition system. Figure 14 is the raw V_f signal for one of the shots. Please note that these are not the shots that

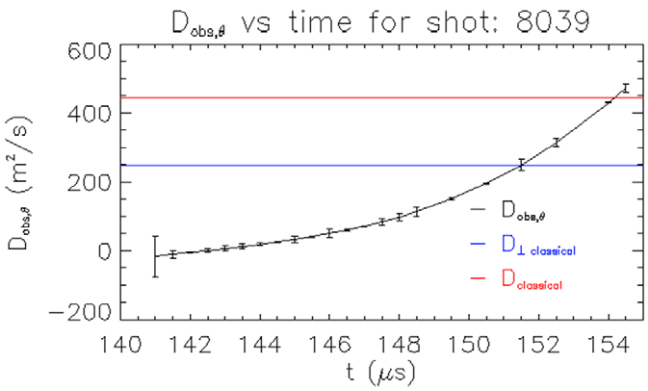

Figure 8. Azimuthal diffusion coefficient as a function of time, based on analysis of tomographic data. The blue and red lines are the values for classical diffusion as calculated in section 2.3 where $B = 200\,\mathrm{G}$ and $0\,\mathrm{G}$ respectively.

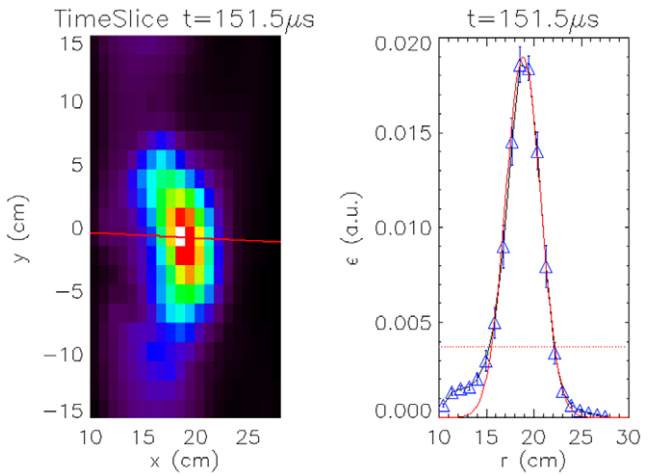

Figure 9. Example of a Gaussian fit along a radial chord (right) and the associated 2D test ion density profile (left). The blue triangles represent the data points and their associated errors. The solid red line is the Gaussian fit (right). The dashed red line is the cutoff value (right). Any data with values below this line are not included in the Gaussian fit.

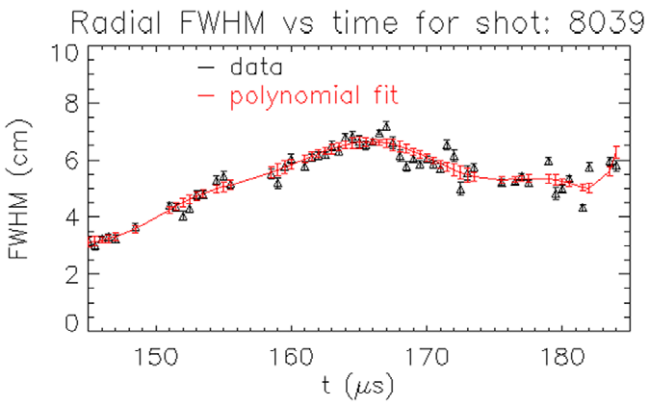

Figure 10. Time evolution of the radial FWHM of the test ion population. Again, the black triangles represent the FWHM from the Gaussian fits at each time slice. The red line is a polynomial fit to the experimentally measured values. Gaps in the data are due to times when the reduced χ^2 of the Gaussian fits are greater than 2.

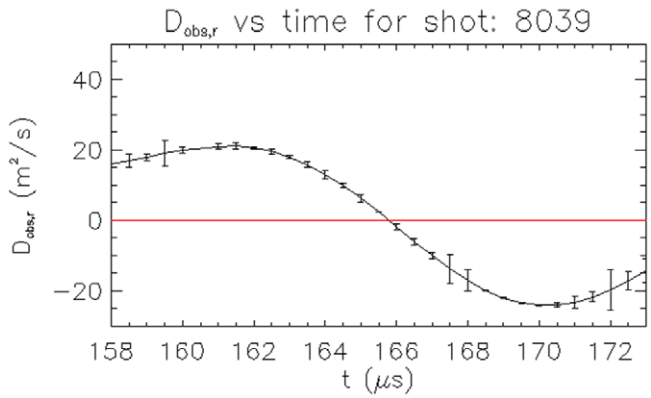

Figure 11. Representation of the observed radial diffusion coefficient as a function of time in the middle of the FRC equilibrium phase, based on analysis of tomographic data.

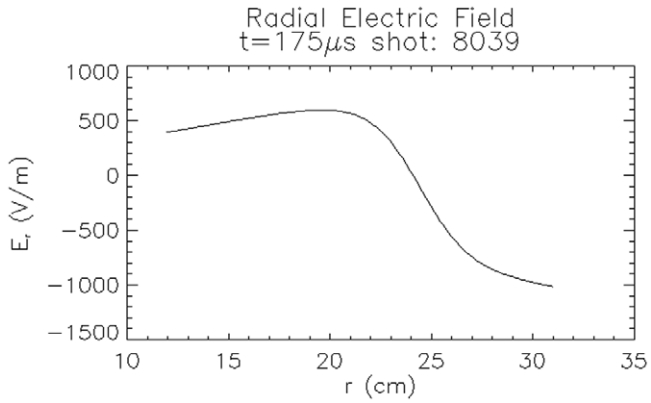

Figure 12. Electric field as predicted by the rigid rotor model based on magnetic field measurements at 175 μs in shot 8039.

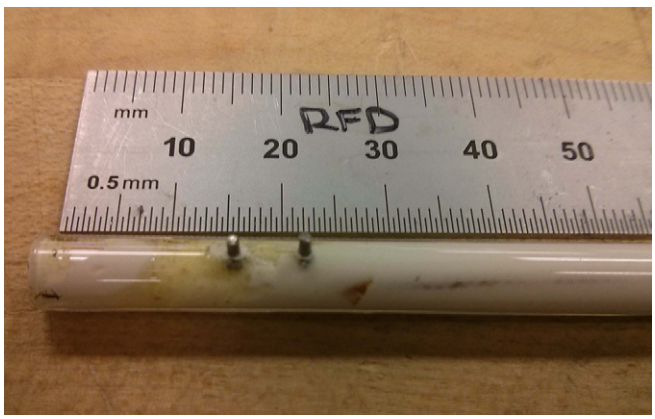

Figure 13. Two-tipped probe used for measuring V_f. In this application V_f is only measured on one tip at a time.

are analyzed using tomography. These data were collected after the tomography experiment had been completed. The shot conditions are as identical to the tomography shots as possible.

The topology of the electric field is theorized to be heavily dependent on the magnetic field topology [4] (section 2.2), especially the position of the magnetic null. The sign of E_r flips at this point (figure 12), or the potential reaches

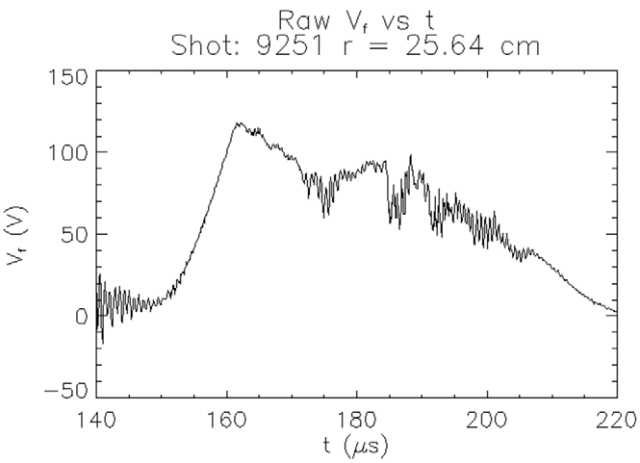

Figure 14. Example of V_f raw signal from a typical shot.

an extremum. Therefore, in performing the analysis of the potential measurements, the position of the probe is taken to be relative to the magnetic null position rather than simply its spatial location alone. This kind of ordering generates very repeatable results (figure 15). This is necessary because the magnetic null position can move several centimeters throughout the shot, even during the equilibrium. From this perspective, V_f can be measured at several positions during a single shot without having to move the probe. This is why there are so many data points in figure 15, each shot supplies about 30 data points.

The magnitude of the potential is well defined for radii that are > -5 cm with respect to the null radius. When the probe tip is more than 10 cm inside of the null, we see a much larger variation in signal (figure 15). There are two perfectly reasonable explanations for this phenomenon. First, the average null radius for these shots is ~20 cm; the radius of the inner boundary is 8.5 cm. It is likely that plasma this close to the wall must be affected. The density is, presumably, much lower near the boundary as well, so fluctuations in the floating potential can easily be more dramatic. Second, the presence of the probe itself may be affecting the measurement. The deeper the tip is inserted into the plasma the larger the surface area exposed to the plasma becomes, and the greater the potential for shorting of field lines, in the vicinity of the probe. Another complication, due to the probe, is that the further it is inserted, the less-precisely the position of the tip is known. This is due to the vacuum interface. The interface is a Wilson seal [22], which means that the probe is only supported by a rubber o-ring. It is possible for the probe to dip a few degrees before it comes into contact with the metal surface that compresses the o-ring. As the lever arm becomes longer (probe is inserted deeper), this small deviation would cause a larger change in the radial position. With all this in mind, it seems to be appropriate to consider the electric field calculated, from these potential measurements, to be valid from ~5 cm inside r_0 to the outer boundary.

With V_f measured we simply take a derivative of the polynomial fit to the data to obtain $E_r(r)$. The confining effect we see in figure 11 implies that E_r should point toward the magnetic null (also the point of highest density) and that is precisely what we see in figure 16.

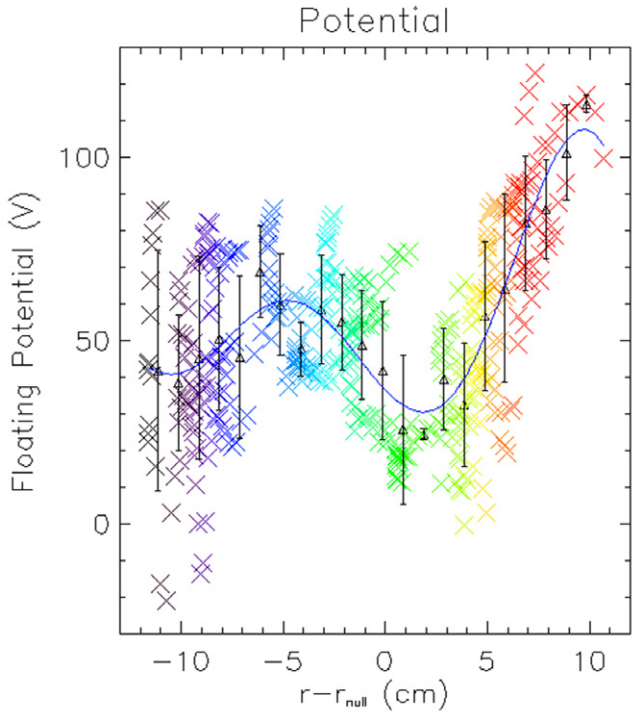

Figure 15. Potential measurements over a series of shots during the equilibrium of the FRC (160–190 μs). The magnetic null position is determined by the midplane B-dot probe. Since the FRC can move during the shot the position of the probe relative to the field null is calculated at every time step. Each × represents a physically measured data point. The data are grouped into 1 cm bins and the error bars represent the standard deviation within the associated bin. The data span each time step for each of the 45 shots. The data are fit to a ninth order polynomial (blue line) that can be differentiated to obtain $E_r(r)$.

5.2. Comparison of multiple calculation methods for E_r

In this section, a comparison of the radial electric field, inferred from floating potential measurements, with the electric fields calculated from $D_{\mathrm{obs},r}$ and magnetic field measurements is presented. The fields are compared as averages over the formation and equilibrium stages of the FRC. The fields predicted by the rigid rotor model and tomographic imaging analysis come from data from the specified shot, and the fields derived from the floating potential measurements are from a different data set.

Figure 17 displays electric field calculations, for shot 8038, averaged over the FRC formation (figure 17(*a*)) and FRC equilibrium (figure 17(*b*)). The black traces represent the rigid rotor model prediction for E_r, these traces are derived, primarily, from magnetic field measurements. The red traces represent the radial electric field which satisfies the flux balancing requirement from section 2.4. These use the tomographic data as well as the magnetic field data. The blue traces represent E_r as calculated from floating potential measurements, as described in section 5.1. Finally, the vertical, purple lines represent the position of the magnetic null. In all

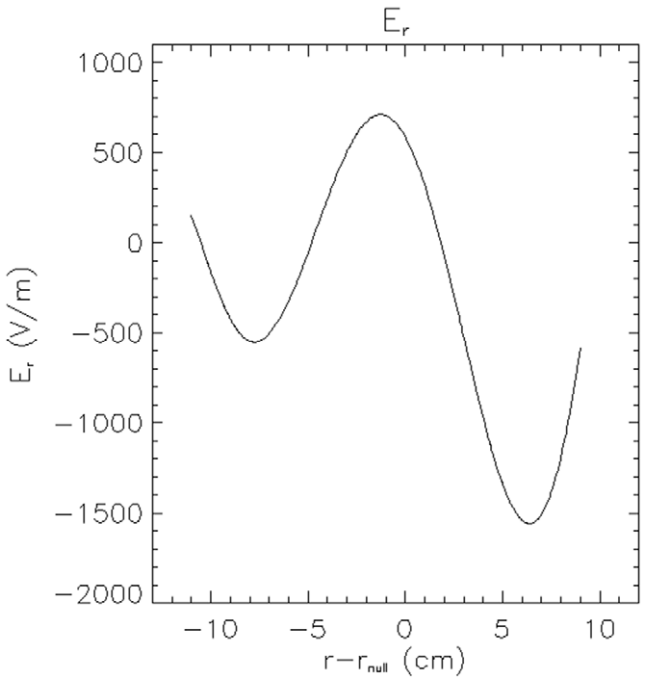

Figure 16. Radial electric field calculated by ninth order polynomial fit to the floating potential data points in figure 15. As expected, the field points toward the magnetic null and is therefore confining for ions. This explains the sub-classical diffusion coefficient measured in section 4.4.

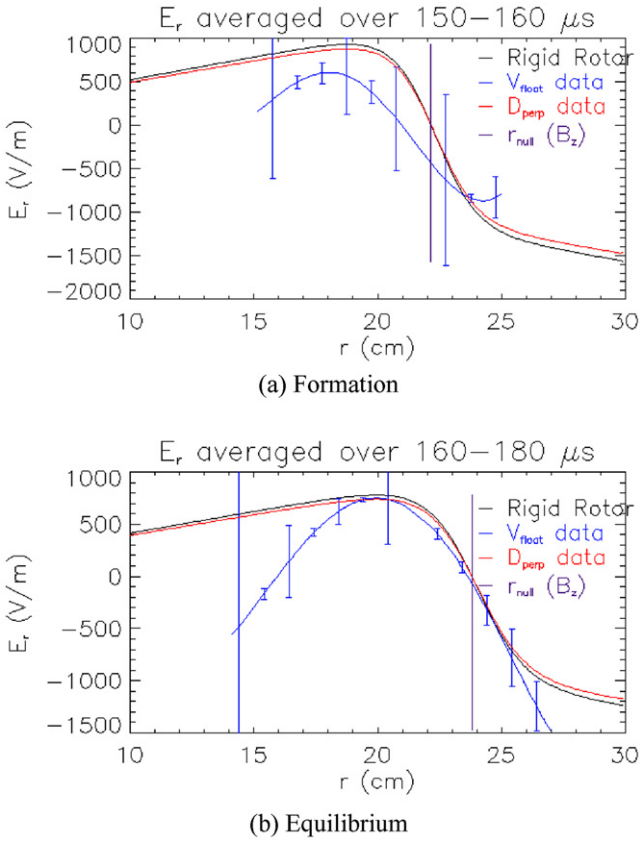

Figure 17. Shot 8038. Comparison of three methods for determining E_r. (*a*) represents E_r during FRC formation and (*b*) represents E_r during FRC equilibrium. Black traces are determined by plasma parameters, magnetic field measurements and the rigid rotor model. Blue traces are determined from direct, floating potential measurements. Red traces are from analysis of the tomographic data. The vertical, purple lines indicate the average position of the magnetic null during the indicated time period.

cases, the values displayed are the average, over the relevant data points, for the specified time window.

The agreement between the three traces is striking. During the formation stage, close to the magnetic null, the slope and magnitude of the traces are nearly identical. All of the signals pass through zero at the same radial location. This means that they all predict the same electric field propelling ions toward the FRC null. This is also the case for the equilibrium phase.

Once we move far enough away (∼5 cm) from the null the V_{float} measurements begin to deviate from the still agreeing rigid rotor and tomography predictions. Away from the null, the plasma density falls off rapidly. Fluctuations in density, from shot-to-shot, make the floating potential much more prone to variation at the plasma edge region. This is exemplified in figure 15, where we see that far inside the null the value of V_{float} is only known with a wide margin of error. Therefore, once we are outside of the dense plasma it makes sense that we will not be able to determine the electric field with high precision, since the measurements are taken over many shots, which are not repeatable in the plasma edge region.

6. Conclusion

The rigid rotor model for field-reversed configurations predicts a radial electric field. This electric field has been inferred using three methods; equilibrium calculation based on magnetic field measurements, impurity transport measurements and floating potential measurements. All three methods give consistent results for both shape and magnitude of the electric field.

Direct observation of test ion particle transport in a collisional FRC showed classical ion diffusion, $\sim 250\,\text{m}^2\,\text{s}^{-1}$. It has also been observed that a radial electric field reduced radial ion flux below classical cross-field diffusive levels during equilibrium. We presume this electric field to be due to the weak and strong levels of magnetization of the ions and electrons, near the magnetic null, respectively. In this collisional regime, the confining electric field is a consequence of ambipolar transport. This particular FRC has very low temperatures, where classical Coulomb collisions dominate diffusive processes during the equilibrium phase. Non-classical diffusion occurs in the formation and collapse phases, and turbulence may contribute substantially to transport in hotter FRCs. In future experiments, it is desirable to perform similar test ion transport studies in hotter, less collisional FRCs in order to determine the level of turbulent transport present. The specifics of diagnostic impurity and method of local introduction would need to be determined based on the plasma parameters of the experiment in question, but the analysis methodology can be applied to any multi-chord light detecting apparatus.

References

[1] Steinhauer L C 2011 Review of field-reversed configurations *Phys. Plasmas* **18** 070501

[2] Guo H Y, Hoffman A L, Milroy R D, Steinhauer L C, Brooks R D, Deards C L, Grossnickle J A, Melnik P, Miller K E and Vlases G C 2008 Improved confinement and current drive of high temperature field reversed configurations in the new translation, confinement, and sustainment upgrade device *Phys. Plasmas* **15** 056101
[3] Rostoker N 1964 Test particle method in kinetic theory of a plasma *Phys. Fluids* **7** 491–8
[4] Rostoker N and Qerushi A 2002 Equilibrium of field reversed configurations with rotation. I. one space dimension and one type of ion *Phys. Plasmas* **9** 3057–67
[5] Camacho J F and Granetz R S 1986 Soft x-ray tomography diagnostic for the alcator C tokamak *Rev. Sci. Instrum.* **57** 417–25
[6] Wenzel K W and Petrasso R D 1990 X-ray imaging arrays for impurity transport studies on the texas experimental tokamak *Rev. Sci. Instrum.* **61** 693–700
[7] McWilliams R and Okubo M 1987 The transport of test ions in a quiet plasma *Phys. Fluids* **30** 2849–54
[8] Harris W S, Trask E, Roche T, Garate E P, Heidbrink W W and McWilliams R 2009 Ion flow measurements and plasma current analysis in the Irvine field reversed configuration *Phys. Plasmas* **16** 112509
[9] Conti F, Wessel F J, Binderbauer M W, Bolte N, Giammanco F, Morehouse M, Qerushi A, Rahman H U, Roche T and Slepchenkov M 2014 Rigid-rotor, field-reversed configuration *Phys. Plasmas* **21** 022511
[10] Gupta D, Bolte N, Gota H, Hayashi R, Kiyashko V, Marsili P, Morehouse M, Primavera S, Roche T and Wessel F 2010 Spectroscopic measurement of ion temperature and ion velocity distributions in the flux-coil generated FRC *Rev. Sci. Instrum.* **81** 10D730
[11] Gota H, Bolte N, Deng B H, Gupta D, Kiyashko V, Knapp K, Mendoza R, Morehouse M, Roche T and Wessel F 2010 Two-chord interferometry using 3.39 μm He–Ne laser on a flux-coil-generated FRC *Rev. Sci. Instrum.* **81** 10D512
[12] Slepchenkov M, Morehouse M, Kiyashko V, Wessel F, Rostoker N, Bolte N and Roche T 2011 Limiter-coil current controller for flux-coil generated FRC *2011 IEEE/NPSS 24th Symp. on Fusion Engineering (SOFE) (26–30 June 2011, Chicago, IL)* pp 1–5
[13] Roche T, Bolte N, Garate E P, Heidbrink W W, McWilliams R and Wessel F 2012 Tomographic imaging system for measuring impurity line emission in a field-reversed configuration *Rev. Sci. Instrum.* **83** 10E503
[14] Pietrzyk Z A, Vlases G C, Brooks R D, Hahn K D and Raman R 1987 Initial results from the coaxial slow source FRC device *Nucl. Fusion* **27** 1478
[15] Pierce W F, Maqueda R J, Brooks R D and Farengo R 1993 Initial results from parallel coil operation of the coaxial slow source field reversed configuration device *Nucl. Fusion* **33** 117
[16] Qerushi A and Neces A 2011 Penetration of the rf field in the RFD experiment *TAE Internal Document*
[17] Huba J D 2011 United States. Office of Naval Research, and Naval Research Laboratory (US) *NRL Plasma Formulary* NRL publication. Naval Research Laboratory
[18] Bellan P M 2008 *Fundamentals of Plasma Physics* (Cambridge: Cambridge University Press)
[19] Fick A 1855 Ueber diffusion *Annal. Phys., Lpz.* **170** 59–86
[20] Anton M, Weisen H, Dutch M J, von der Linden W, Buhlmann F, Chavan R, Marletaz B, Marmillod P and Paris P 1996 X-ray tomography on the TCV tokamak *Plasma Phys. Control. Fusion* **38** 1849–78
[21] Press W, Teukolsky S, Vetterling W and Flannery B 1992 *Numerical Recipes in C* 2nd edn (Cambridge: Cambridge University Press)
[22] Roth A and Roth A 1966 *Vacuum Sealing Techniques* (New York: Pergamon)